

First observation of the thermal Sunyaev-Zel'dovich effect with Kinetic Inductance Detectors

R. Adam¹, B. Comis¹, J. F. Macías-Pérez¹, A. Adane², P. Ade³, P. André⁴, A. Beelen⁵, B. Belier⁶, A. Benoît⁷, A. Bideaud³, N. Billot⁸, N. Boudou⁷, O. Bourrion¹, M. Calvo⁷, A. Catalano¹, G. Coiffard², A. D'Addabbo⁷, F.-X. Désert⁹, S. Doyle³, J. Goupy⁷, C. Kramer⁸, S. Leclercq², J. Martino⁵, P. Mauskopf³, F. Mayet¹, A. Monfardini⁷, F. Pajot⁵, E. Pascale³, L. Perotto¹, E. Pointecouteau^{10,11}, N. Ponthieu⁹, V. Revéret⁴, L. Rodriguez⁴, G. Savini¹², K. Schuster², A. Sievers⁸, C. Tucker³, and R. Zylka²

¹ Laboratoire de Physique Subatomique et de Cosmologie, Université Joseph Fourier Grenoble 1, CNRS/IN2P3, Institut Polytechnique de Grenoble, 53, rue des Martyrs, Grenoble, France

² Institut de RadioAstronomie Millimétrique (IRAM), Grenoble, France

³ Astronomy Instrumentation Group, University of Cardiff, UK

⁴ Laboratoire AIM, CEA/IRFU, CNRS/INSU, Université Paris Diderot, CEA-Saclay, 91191 Gif-Sur-Yvette, France

⁵ Institut d'Astrophysique Spatiale (IAS), CNRS and Université Paris Sud, Orsay, France

⁶ Institut d'Electronique Fondamentale (IEF), Université Paris Sud, Orsay, France

⁷ Institut Néel, CNRS and Université de Grenoble, France

⁸ Institut de RadioAstronomie Millimétrique (IRAM), Granada, Spain

⁹ Institut de Planétologie et d'Astrophysique de Grenoble (IPAG), CNRS and Université de Grenoble, France

¹⁰ Université de Toulouse, UPS-OMP, Institut de Recherche en Astrophysique et Planétologie (IRAP), Toulouse, France

¹¹ CNRS, IRAP, 9 Av. colonel Roche, BP 44346, F-31028 Toulouse cedex 4, France

¹² University College London, Department of Physics and Astronomy, Gower Street, London WC1E 6BT, UK

Received October 23, 2013 / Accepted –

Abstract

Context. Clusters of galaxies provide precious informations on the evolution of the Universe and large scale structures. Recent cluster observations via the thermal Sunyaev-Zeldovich (tSZ) effect have proven to be a powerful tool to detect and study them. In this context, high resolution tSZ observations (\sim tens of arcsec) are of particular interest to probe intermediate and high redshift clusters. **Aims.** Such observations will be carried out with the millimeter dual-band *NIKA2* camera, based on Kinetic Inductance Detectors (KIDs) and to be installed at the IRAM 30-meter telescope in 2015. To demonstrate the potential of such an instrument, we present tSZ observations with the *NIKA* camera prototype, consisting of two arrays of 132 and 224 detectors observing at 140 and 240 GHz with a 18.5 and 12.5 arcsec angular resolution, respectively.

Methods. The cluster RX J1347.5-1145 was observed simultaneously at 140 and 240 GHz. We used a spectral decorrelation technique to remove the atmospheric noise and obtain a map of the cluster at 140 GHz. The efficiency of this procedure has been characterized through realistic simulations of the observations.

Results. The obtained 140 GHz map presents a decrement at the cluster position consistent with the tSZ nature of the signal. We used this map to study the pressure distribution of the cluster by fitting a gNFW model to the data. Subtracting this model from the map, we confirm that RX J1347.5-1145 is an ongoing merger, in agreement and complementary to previous tSZ and X-ray observations.

Conclusions. For the first time, we demonstrate the tSZ capability of KIDs based instruments. The *NIKA2* camera, with \sim 5000 detectors and a 6.5 arcmin field of view, will be a well-suited instrument for in-depth studies of the Intra Cluster Medium from intermediate to distant clusters and so for the follow-up of recently detected clusters by the *Planck* satellite.

Key words. Instrumentation: detectors – Techniques: high angular resolution – Galaxies: clusters: individual: RX J1347.5-1145; intracluster medium

1. Introduction

Galaxy clusters are the largest gravitationally bound objects in the Universe. Their formation strongly depends on the content and the history of the Universe, within the framework of a bottom-up scenario (Kravtsov & Borgani 2012), *i.e.* merging of small clusters to form larger ones. They are classically probed using X-ray (Böhringer & Werner 2010), via bremsstrahlung emission of the electrons in the intra cluster medium (ICM), but also measured in the optical (Gal 2006), radio (Feretti et al. 2012), infrared (Oliver et al. 2012) and lensing of background galaxies (Kneib & Natarajan 2011) observations. The thermal

Sunyaev-Zel'dovich (tSZ) effect (Sunyaev & Zel'dovich 1972, 1980), which consists in the inverse Compton scatter of Cosmic Microwave Background (CMB) photons on hot electrons in the ICM, can be used as a complementary and powerful method for probing galaxy clusters (see Birkinshaw 1999; Carlstrom et al. 2002, for a detailed review on the tSZ effect). Three dimensional information on the cluster may be inferred using the characteristic dependences on the ICM properties of X-ray (sensitive to the density squared) and tSZ (sensitive to the integrated pressure along the line-of-sight), giving a more accurate picture than X-ray or tSZ alone, in particular in the case of merging systems (Basu et al. 2010). In addition, unlike the other observational approaches, the tSZ flux does only depend on the angular size of

Send offprint requests to: R. Adam - adam@lpsc.in2p3.fr

the observed cluster and not on the distance to the source. High angular resolution tSZ observations are therefore of particular interest to probe structure formation at high redshift.

The resolutions of the main current instruments measuring the tSZ effect are of the order of the arcmin: larger than 5 arcmin for the *Planck* satellite (Planck Collaboration et al. 2013b) and about 1 arcmin for the South Pole Telescope (*SPT*; Carlstrom et al. 2011) and the Atacama Cosmology Telescope (*ACT*; Kosowsky 2003). Higher resolution instruments such as *MUSTANG* (~ 8 arcsec resolution at 90 GHz; Mason et al. 2010; Korngut et al. 2011) may suffer from filtering of large scale structures due to the atmospheric noise removal when observing at a single frequency band. High redshift tSZ observations therefore need a new generation of instruments. The New IRAM KID Arrays (*NIKA*) is a prototype of a high resolution camera based on Kinetic Inductance Detectors (KIDs) (Day et al. 2003; Calvo et al. 2010), in development for millimeter wave astronomy (Monfardini et al. 2011). It consists of two arrays of 132 and 224 detectors, observing at 140 and 240 GHz, with resolutions of 12.5 and 18.5 arcsec. Due to the characteristic spectral distortion of the CMB photons induced by the tSZ effect, *NIKA* appears to be an ideal instrument for high resolution tSZ observations. Indeed, the tSZ signal is strongly negative at 140 GHz and positive but close to zero at 240 GHz. The *NIKA* prototype has already been successfully tested during four observation campaigns (Monfardini et al. 2010, 2011) at the Institut de Radio Astronomie Millimétrique (IRAM) 30-meter telescope at Pico Veleta, Granada, Spain. They allowed us to demonstrate performance comparable to state-of-the-art bolometer arrays developed to date for these wavelengths, such as *GISMO* (Staguhn et al. 2008). The final camera, *NIKA2*, will contain 1000 and 4000 detectors at 140 and 240 GHz, and should be operational in 2015.

We report here the first observation of a galaxy cluster via the tSZ effect using the *NIKA* prototype. It has been imaged during the fifth observation campaign of *NIKA*, in November 2012. The targeted source is the massive intermediate redshift galaxy cluster RX J1347.5-1145 at $z = 0.4516$. It has been selected for its tSZ intensity and angular size, comparable to the field of view of the *NIKA* prototype. Moreover, RX J1347.5-1145 is known to be a complex merging system that we aim at characterizing furthermore, with respect to previous works, at scales in the range 20 – 200 arcsec.

This paper is organized as follows. In Sect. 2, we give the status of the previous observations of RX J1347.5-1145. In Sect. 3, we provide a brief description of the *NIKA* camera and give an overview of the observations carried out during the November 2012 campaign at the IRAM 30-meter telescope. Sect. 4 describes the tSZ dedicated data analysis and its validation on simulations is reported in Sect. 5. We present in Sect. 6 the map of RX J1347.5-1145 and the results on the profile for this cluster of galaxies. These results are compared to other experiments in Sect. 7. Throughout this paper we assume a flat Λ CDM cosmology according to the last *Planck* results (Planck Collaboration et al. 2013d) with $H_0 = 67.11 \text{ km.s}^{-1}.\text{Mpc}^{-1}$, $\Omega_M = 0.3175$, and $\Omega_\Lambda = 0.6825$.

2. Previous observations of RX J1347.5-1145

RX J1347.5-1145 is one of the very few clusters that has been intensively observed in many wavelengths, including sub-arcmin resolution. It is a massive intermediate redshift galaxy cluster at $z = 0.4516$ undergoing a merging event.

It is the most luminous X-ray cluster ever observed. It was discovered in the *ROSAT* X-ray all-sky survey and has been the object of many studies in X-ray (Schindler et al. 1995, 1997; Allen et al. 2002; Gitti & Schindler 2004, 2005; Gitti et al. 2007b,a; Ota et al. 2008), optical (Cohen & Kneib 2002; Verdugo et al. 2012), tSZ (Pointecouteau et al. 1999, 2001; Komatsu et al. 2001; Kitayama et al. 2004; Mason et al. 2010; Korngut et al. 2011; Plagge et al. 2012), and multi-wavelengths analysis (Bradač et al. 2008; Miranda et al. 2008; Johnson et al. 2012). From X-ray observations, this cluster was thought to be a dynamically old relaxed cool-core cluster with an extremely strong cooling flow, due to its very spherical morphology and peaked X-ray profile (*ROSAT*; Schindler et al. 1995, 1997). However, high angular resolution tSZ observations have proved RX J1347.5-1145 to be an ongoing merger from the shift between the X-ray and tSZ signal maxima (Pointecouteau et al. 1999; Komatsu et al. 2001; Kitayama et al. 2004). As a matter of fact, it is a perfect illustration of the complementarity of tSZ and X-ray (and other wavelengths) observations.

High resolution tSZ maps of RX J1347.5-1145, such as the 90 GHz 8 arcsec (smoothed to 10 arcsec) resolution map of *MUSTANG* (Mason et al. 2010), have confirmed the presence of a strong South East (SE) extension. It is interpreted as being due to hot gas heated by the merging of a sub cluster crossing the main, originally relaxed system, from the South to the North East (NE), perpendicularly to the line of sight. The SE extension coincides with a radio mini-halo (Gitti et al. 2007a) which indicates the presence of non-thermal electrons, underlying a non-thermal contribution to the total pressure. Optical observations have also confirmed this scenario with the detection of a massive elliptical galaxy located 20 arcsec on the east side of the X-ray center, while the central elliptical galaxy of the main cluster remains at the X-ray peak location (Cohen & Kneib 2002). More recent X-ray (*Chandra*; Allen et al. 2002) and lensing (Miranda et al. 2008) observations also agree with this interpretation.

The temperature profile of RX J1347.5-1145 varies from ~ 6 keV in its core to ~ 20 keV at 80 arcsec and decreases to ~ 9 keV on the outer part of the cluster (120–300 arcsec from the core). The maximum temperature is located at the SE extension, reaching $k_B T_e \sim 25$ keV (Ota et al. 2008). The Compton y parameter has been measured to be $y_{\text{max}} \approx 10^{-3}$ (Pointecouteau et al. 1999).

Finally, RX J1347.5-1145 hosts a well known radio source within 3 arcsec of the X-ray center, in the central elliptical galaxy. This has to be taken into account in the tSZ analysis. According to Pointecouteau et al. (2001), the source follows the spectrum $F_\nu = (77.8 \pm 1.7) \nu_{\text{GHz}}^{-0.58 \pm 0.01} \text{ mJy}$. Hence, for *NIKA* it corresponds to 4.4 ± 0.3 and 3.2 ± 0.2 mJy at 140 and 240 GHz respectively.

3. Observations with *NIKA*

3.1. Brief overview of the *NIKA* camera during the campaign of November 2012

NIKA consists of two arrays of Kinetic Inductance Detectors (KIDs) with maximum transmission at about 140 and 240 GHz with respective resolutions (FWHM) of 18.5 and 12.5 arcsec and effective fields of view of 1.8 and 1.0 arcmin. The FWHM band-pass are 43 and 57 GHz wide respectively. In this particular campaign of November 2012, the first band (140 GHz) was used with 127 detectors having a mean effective sensitivity of $29 \text{ mJy.s}^{1/2}$ per beam ($19 \text{ mJy.s}^{1/2}$ per beam for the best 20% of all pixels) and the second band (240 GHz), had 91 detectors with a mean ef-

	Nov. 21 st	Nov. 22 nd	Nov. 23 rd
$\tau_{140 \text{ GHz}}$	0.14	0.18	0.053
$\tau_{240 \text{ GHz}}$	0.17	0.22	0.046
Time range	8:27 am to 11:43 am	8:16 am to 12:01 pm	8:11 am to 10:59 am
Integration time	2 hrs 29 min	3 hrs 00 min	2 hrs 29 min
Unflagged integration time	50 min	2 hrs 35 min	2 hrs 23 min

Table 1. Mean zenith opacity, on-source integration time and period of the day for the three days of the campaign of November 2012 where we observed RX J1347.5-1145. The total integrated time used is 5 hrs 47 min. The mean opacity ratio is $\tau_{240 \text{ GHz}} / \tau_{140 \text{ GHz}} \approx 1.2$

fective sensitivity of $55 \text{ mJy.s}^{1/2}$ per beam ($37 \text{ mJy.s}^{1/2}$ per beam for the best 20% of all pixels). This rather sensitivity worse than expected and the small number of available detectors of the second band, in the case of this campaign, is due to the disfunction of a cold amplifier. Using only eight detectors of the 240 GHz array, we obtain the expected mean effective sensitivity measured to be $22 \text{ mJy.s}^{1/2}$ per beam.

Unlike traditional instruments that use bolometers, *NIKA* uses KIDs. KIDs are superconducting resonators whose resonance frequency ($\sim 1\text{--}2.5 \text{ GHz}$) changes with the absorbed optical power (see for example Swenson et al. 2010). They can be modeled by a complex transfer function with real part I (In-phase) and imaginary part Q (Quadrature) (Grabovskij et al. 2008), measured as a function of time. These quantities can then be used to reconstruct the shift of the resonance frequency which is to first order proportional to the absorbed optical power with accurate photometry (Calvo et al. 2012).

The KIDs used here are Hilbert dual-polarization design LEKID pixels (Lumped Element KID; Doyle et al. 2008; Roesch et al. 2012) realized on a few hundred μm thickness high resistivity silicon substrate. The pitch between pixels is 2.3 mm at 140 GHz and 1.6 mm at 240 GHz . This corresponds to an effective focal plane sampling of $0.77 \text{ F}\lambda$ and $0.8 \text{ F}\lambda$ at 140 and 240 GHz respectively. The detectors are cooled down to about 100 mK with a $^4\text{He} - ^3\text{He}$ dilution cryostat.

More details on the *NIKA* prototype setup can be found in *NIKA* Collaboration (2013).

3.2. Observing strategy of the targeted galaxy clusters

Galaxy clusters are weak extended sources when seen through the tSZ effect, making their observations rather challenging. The target cluster has been chosen to be among the most luminous tSZ sources in the sky. It is also compact enough to have an angular size comparable to the field of view of the camera. This target is the intermediate redshift cluster of galaxies RX J1347.5-1145 at $z = 0.4516$.

As shown in Fig. 1, the cluster signal is scan-modulated but there is no wobbling involved. Raster scans are made of constant elevation subscans or constant azimuth subscans. For the latter, only the left part of the field was covered due to software mistake. Both of them are $6 \text{ min } 20 \text{ s}$ scans made of 19 subscans separated by 10 arcsec steps. Scans along the azimuth direction are centered on (R.A., Dec) = (13h 47m 32s, $-11^\circ 45' 42''$) sampling a rectangular region of $360 \times 180 \text{ arcsec}^2$ (azimuth \times elevation), while scans along the elevation sample a region of $180 \times 180 \text{ arcsec}^2$ centered on a point 90 arcsec away from (13h 47m 32s, $-11^\circ 45' 42''$), which rotates with the parallactic angle. The scan velocity is about 15 arcsec.s^{-1} . The detailed integration times are given in Tab. 1 with the corresponding atmospheric opacities.

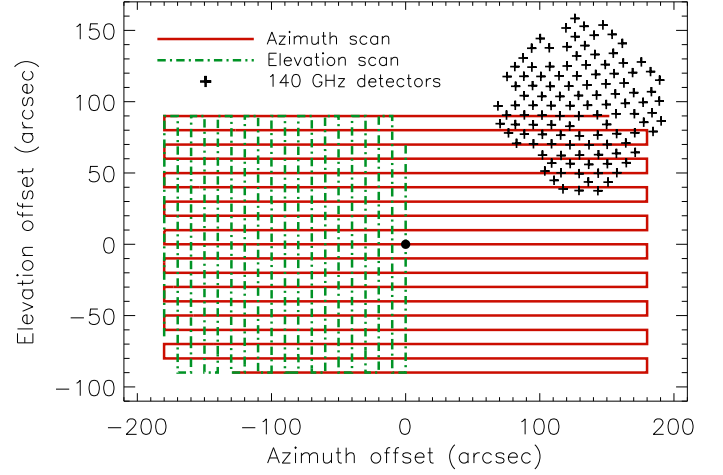


Figure 1. Elevation (dashed green) and azimuth (solid red) offsets scans. The center is represented by a black circle and has coordinates (R.A., Dec) = (13h 47m 32s, $-11^\circ 45' 42''$). The 140 GHz array is also represented by the black crosses that correspond to the position of each KID in the focal plane (gaps in the array correspond to invalid detectors).

3.3. Pointing, calibration, bandpasses and beam

Uranus observations were used to reconstruct beam maps (projection of the array in the sky and measure of individual detector beams) for both wavelengths. Nearby quasars were used for determining pointing corrections. The pointing root mean square error is estimated to be $\sim 3 \text{ arcsec}$ (*NIKA* Collaboration 2013). This is small compared to the beam and has a negligible impact in the case of extended sources such as RX J1347.5-1145.

We also used Uranus for absolute point source flux calibration. The flux of the planet was inferred from a frequency dependent model of the planet brightness temperature taken from Planck Collaboration et al. (2013c). Typically we obtain brightness temperatures of 113 K at 140 GHz and 94 K at 240 GHz for Uranus¹. This model is integrated over the *NIKA* bandpasses for each channel and it is assumed to be accurate at the level of 5%. The actual angular size of the planet at the time of the observations was accounted for. The final absolute calibration factor is obtained by fitting a gaussian of fixed angular size on the reconstructed maps of Uranus (representing the main beam).

The observed sky maps (also for Uranus maps prior to calibration) are corrected for atmospheric absorption using elevation scans – skydips (see *NIKA* Collaboration 2013, for fur-

¹ Moreno, R. 2010, Uranus planetary brightness temperature tabulation. Tech. rep., ESA Herschel Science Center, available from <ftp://ftp.sciops.esa.int/pub/hsc-calibration/PlanetaryModels/ESA2>.

Systematic uncertainty	Error percentage
Brightness temperature model	5%
Point source calibration	15%
Secondary beams fraction	45% \pm 10 %
Bandpasses	2%

Table 2. Main contributions to the absolute error of the *NIKA* data for the 140 GHz band.

ther details). In our case, the resonance frequencies of the detectors are measured versus the optical load, which depends on the zenith opacity and the elevation. This gives the zenith opacity as a function of the resonance frequency of the detectors, which is measured for each scan. The opacity can then be corrected to good accuracy by accounting for the air mass at the elevation of the source. Furthermore, different atmospheric conditions lead to changes in the beam pattern of the instrument affecting also the absolute calibration accuracy (NIKA Collaboration 2013). From the dispersion of the recovered flux of Uranus, which was observed several times with different opacities during the campaign, we estimate an overall accuracy of 15% (NIKA Collaboration 2013) for the calibration procedure.

Scales larger than 180 arcsec, the scan size, were not measured with *NIKA*. Integrating the Uranus flux up to 100 arcsec, we observe that the total solid angle covered by the beam is larger than the main beam (obtained from the Gaussian fit) by a factor of 1.32. Using the IRAM 30-meter beam pattern from Greve et al. (1998)² we extrapolate the angular profile of the beam from 100 arcsec to 180 arcsec, and we obtain a factor equal to 1.45. From the dispersion over different observations of Uranus we estimate the uncertainties on the solid angle of the main beam to be of the order of 4 % and of 10 % for the full beam when including uncertainties on the side lobes.

To summarize, the list of the main systematic uncertainties in the 140 GHz band are listed in Tab. 2. The total calibration uncertainty on the final data at the map level is estimated to be 16%.

4. Thermal Sunyaev-Zel'dovich dedicated data analysis and map-making

4.1. Thermal Sunyaev-Zel'dovich data

In the non-relativistic limit, the tSZ effect results in a distortion of the CMB black-body spectrum whose frequency dependence is given by (Birkinshaw 1999)

$$f(x) = x \coth\left(\frac{x}{2}\right) - 4 \quad (1)$$

where $x = \frac{h\nu}{k_B T_{\text{CMB}}}$ is the dimensionless frequency; h is the Planck constant, k_B the Boltzmann constant, ν the observation frequency and T_{CMB} the temperature of the CMB. The induced temperature anisotropy reads

$$\frac{\delta T_{\text{CMB}}}{T_{\text{CMB}}} = y f(x) \quad (2)$$

² See also Kramer, Penalver, Greve 2013, "Improvement of the IRAM 30m telescope beam pattern" available at <http://www.iram.es/IRAMES/mainWiki/CalibrationPapers> for more recent measurements of the IRAM 30-meter beam pattern.

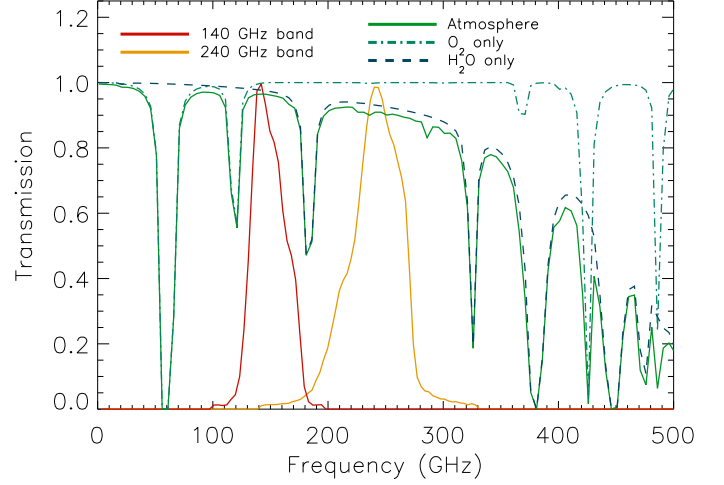


Figure 2. Normalized 140 GHz (solid red line) and 240 GHz (solid orange line) instrumental bandpasses. The total atmospheric transmission is also given as a solid green line for 1 mm of precipitable water vapor according to the Pardo model (Pardo et al. 2002). The oxygen (dash-dotted light blue) and the water vapor (dashed dark blue) contributions are represented.

where y is the Compton parameter which measures the integrated electronic pressure P_e along the line-of-sight.

$$y = \frac{\sigma_T}{m_e c^2} \int P_e dl \quad (3)$$

σ_T is the Thomson cross section, m_e is the electron mass and c the speed of light. The tSZ spectral distortion is null at 217 GHz, negative below and positive above.

The unit conversion coefficients between Jansky per beam and the Compton parameter y are -11.8 ± 1.2 and $+2.2 \pm 0.6$ respectively at 140 and 240 GHz for the *NIKA* prototype. They are computed taking into account the overall transmission of the instrument and the measured total beam with their respective errors (y is converted to δT_{CMB} using Eq. 2 and then converted to flux (Jy/beam) using the angular coverage of the beam). They are given here assuming a pure non-relativistic tSZ spectrum.

As the expected tSZ signal is small (up to $y \sim 10^{-3}$), the *NIKA* data are dominated by instrumental noise and atmospheric emission. We model the signal measured by a KID k , operating at the observing frequency band ν_b (140 GHz or 240 GHz) as:

$$d_k(\nu_b, t) = S_k(\nu_b, t) + N_k(t) + E(\nu_b, t) + A(\nu_b, t) \quad (4)$$

The astrophysical signal (essentially tSZ) $S_k(\nu_b, t)$ depends on time via the scanning strategy, on the frequency band (Eq. 2) and on the detector k via its location in the projection of the array in the sky. $N_k(t)$ is the intrinsic detector noise limiting the sensitivities given in Sect. 3.1. The correlated electronic noise, $E(\nu_b, t)$, is well characterized by an identical common-mode for the detectors of the same band (Bourrion et al. 2011). As we use independent readout electronics for the two bands, the electronic noise is uncorrelated between bands. Finally, by splitting the frequency and time dependences, the atmospheric contribution can be modeled as

$$A(\nu_b, t) = a_{\text{H}_2\text{O}}^{\text{el}}(\nu_b) A_{\text{H}_2\text{O}}^{\text{el}}(t) + a_{\text{O}_2}^{\text{el}}(\nu_b) A_{\text{O}_2}^{\text{el}}(t) + a_{\text{H}_2\text{O}}^{\text{fluc}}(\nu_b) A_{\text{H}_2\text{O}}^{\text{fluc}}(t) \quad (5)$$

The first and the second terms give the emission change of water vapor and oxygen due to the variation of the airmass with

the elevation. The third term, $a_{\text{H}_2\text{O}}^{\text{fluc}}(\nu_b) A_{\text{H}_2\text{O}}^{\text{fluc}}(t)$, gives the emission change due to inhomogeneities in the water vapor distribution. Note that $a_{\text{O}_2}^{\text{fluc}}$ is implicitly set to zero because we assume that the oxygen is locally very homogeneous in the atmosphere. It is important to notice that the two bands are not sensitive to the same atmospheric components. The 140 GHz band is rather sensitive to the O_2 118 GHz line while the 240 GHz band is almost only sensitive to water vapor (Pardo et al. 2002), such that $\frac{a_{\text{O}_2}^{\text{el}}(140 \text{ GHz})}{a_{\text{H}_2\text{O}}^{\text{el}}(140 \text{ GHz})} \gg \frac{a_{\text{O}_2}^{\text{el}}(240 \text{ GHz})}{a_{\text{H}_2\text{O}}^{\text{el}}(240 \text{ GHz})}$. This can be observed in Fig. 2 where we show the bandpasses of the *NIKA* prototype in red (140 GHz) and orange (240 GHz). The atmospheric transmission is given for the oxygen and water vapor contributions in light blue dash-dotted line and dark blue dashed line respectively and the overall atmospheric transmission is given as a green solid line, according to the Pardo model (Pardo et al. 2002). Trace constituents are neglected here (e.g. ozone).

4.2. Time Ordered Data analysis

The main steps of the processing of the Time Ordered Data (TOD) are:

- Loading raw data, including the telescope parameters, the reconstruction of the projection of the array in the sky and the atmospheric opacity.
- TOD astrophysical calibration, including opacity correction.
- Flagging of invalid detectors.
- Flagging of cosmic ray impacts on the detectors.
- Atmospheric and electronic noise decorrelation.
- Low frequency filtering and notch filtering of lines produced by the pulse tube of the cryostat.
- Mapmaking using inverse variance weighting.

In the following, we give details on specific points of the analysis.

4.2.1. Raw data

The raw TOD correspond to the real ($I_k(t)$, in-phase) and imaginary ($Q_k(t)$, quadrature) parts of the transfer function of the system (array and transmission line) sampled on predefined frequency tones k at an acquisition rate of 23.842 Hz. We also compute the average modulation of these quantities with respect to the injected frequency (typically a few kHz), noted $\delta I_k(t)$ and $\delta Q_k(t)$. These four quantities are used to reconstruct the shift of the resonance frequency $\delta f_{0k}(t)$, which probes the optical power absorbed by a detector (see Calvo et al. 2012, for more details). In order to monitor the electronic noise and possible variations of the transfer function of the transmission line, the latter is also sampled with tones that are placed off-resonance (with no correspondence to any detector), thus insensitive to optical power.

In the case of the *NIKA* prototype, some detectors are subject to cross talk. For now these KIDs are rejected. Bad detectors are flagged on the basis of the statistical properties of their noise. We use in particular skewness and kurtosis tests, in addition to tests of the stationarity of the noise. Some TODs affected by baseline jumps due to the coupling with ambient magnetic fields are also excluded. These rejected tones will not be used in the following. In the case of the observation of RX J1347.5-1145, the number of detectors used in the analysis are 81 at 140 GHz and 45 at 240 GHz.

4.2.2. Calibration

The shift of the resonance frequency is computed for each detector. The absolute calibration from resonance frequency to flux density is applied to these TODs. The beam is measured with Uranus observations in atmospheric conditions similar to RX J1347.5-1145. It has been fitted with a gaussian function of FWHM equal to 12.5 and 18.5 arcsec at 240 and 140 GHz respectively. An opacity correction is performed by multiplying the data by $\exp(\tau_{\nu_b}/\sin(\langle el \rangle))$, where el is the elevation of the telescope. The calculation of the opacity is based on skydips as briefly described in Sect. 3.3 (for more details, see *NIKA* Collaboration 2013).

4.2.3. Glitch removal

Cosmic rays hitting the instrument induce glitches in the data. The time response of KIDs is negligible compared to the sampling frequency such that a cosmic ray impact appears as a peak on a single data sample in the TOD. We detect about four glitches per minute. They are removed from the $\delta f_{0k}(t)$ TODs by flagging peaks above five times the standard deviation of the considered TOD. The TODs are flagged and interpolated at the glitch locations in order not to affect the decorrelation. These flagged data are not projected onto maps.

4.2.4. Dual-band decorrelation

At first order, the atmospheric contribution $A(\nu_b, t)$ is essentially due to water vapor. It is therefore the same for the two frequency bands, up to an amplitude factor $A(240 \text{ GHz}, t)/A(140 \text{ GHz}, t) \approx 5$ – i.e. $a_{\text{O}_2}^{\text{el/fluc}}(\nu_b)$ are small compared to $a_{\text{H}_2\text{O}}^{\text{el/fluc}}(\nu_b)$. Therefore, we use the 240 GHz data, in which the tSZ signal is negligible, to build the atmosphere template that we remove from the 140 GHz data in each subscan of each TOD individually, by template fitting. The atmosphere is dominant only at low frequencies, following a $1/f$ noise like power spectrum. As shown on the right panel of Fig. 3, the atmospheric contribution induces long term drifts in the TOD (red line). These drifts correspond to the $1/f$ noise like spectrum with knee frequency at about 1 Hz (red line, right panel). Therefore, we apply a low-pass filter to this template. This removes most of the correlated electronic noise contained in the 240 GHz band – $E(240 \text{ GHz}, t)$ – but not present in the 140 GHz data. Moreover, this technique has the effect of reducing the intrinsic high noise level of the 240 GHz band, specific to the November 2012 *NIKA* data, that could lower the sensitivity of the 140 GHz cleaned data. The low-pass filter does not affect frequencies smaller than 1.5 Hz and sets frequencies larger than 2 Hz to zero. Frequencies between 1.5 and 2 Hz are progressively attenuated using a cosine squared cutoff.

Similarly, we build a template with a high-pass filtered common-mode made from the 140 GHz TODs. The filter is the complement to the previous low-pass filter such that their sum is equal to one for all frequencies. Once the template is fitted to the individual subsamples of each TOD, the correlated electronic noise $E(140 \text{ GHz}, t)$ is removed at frequencies larger than the cutoff. Note that this does not affect much the tSZ signal because at these frequencies, it is not correlated between detectors due to the different position of the KIDs in the projection of the array in the sky: 2 Hz corresponds to about 8 arcsec with our scan speed (~ 15 arcsec per second).

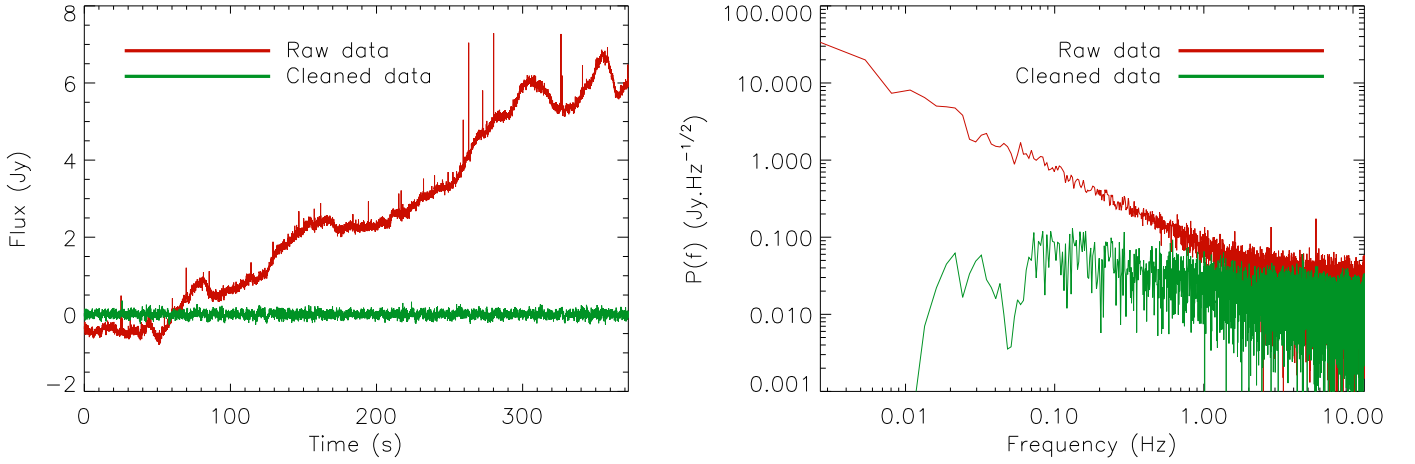


Figure 3. TOD (left) and their power spectra (right) for a given detector. They correspond to the calibrated TOD before (red) and after (green) the electronic and atmospheric noise decorrelation. The TODs are dominated by the atmospheric noise at low frequencies which is responsible for the slow variations in the red TOD and the obvious rise of noise below ~ 1 Hz on the red power spectrum. The glitches can be seen as spikes in the TODs but have been removed before computing the power spectra. Pulse tube frequency lines appear in the power spectrum (e.g. the ~ 6 Hz line in the raw power spectrum) and are notch filtered. The electronic noise dominates at frequencies between ~ 1 and 5 Hz in the power spectrum before the decorrelation.

Finally, we fit and remove from the TODs a template that follows the elevation of the telescope. Indeed, the oxygen component of the atmosphere is ignored in the dual-band decorrelation and appears as a residual proportional to the elevation of the telescope. Notice that the positive bias introduced in the 140 GHz data by the tSZ signal present at 240 GHz, already smaller by a factor of ~ 6 (Eq. 1 and 2), is reduced by a factor of ≈ 5 when scaled down to 140 GHz and is therefore negligible. Moreover, since the opacity is larger at 240 GHz than 140 GHz, the bias is even more reduced, by a factor of few percents. The kinematic Sunyaev-Zel'dovich (kSZ) effect, due to the overall motion of a cluster (or its components) with respect to the CMB reference frame, follows a pure CMB black-body spectrum that is non-zero around 240 GHz and might bias our analysis. However, kSZ signal would also be reduced by a factor of ~ 5 such that the flux at 240 GHz would have to be larger than half the tSZ flux at 140 GHz to account for a non-negligible bias. This is not the case even for the most extreme clusters such as MACS J0717.5+3745 (Mroczkowski et al. 2012). Therefore, any kSZ signal present at 240 GHz is neglected in the following analysis.

4.2.5. Fourier filtering

Frequency lines (e.g. at ~ 6 Hz) are induced by the pulse tube of the cryostat and observed in the TOD power spectra (see Fig. 3, right panel). They are flagged and set to zero. In addition, we apply a high-pass filter to remove correlated noise at frequencies lower than the subscan because no tSZ signal is present there. We also remove low frequency (below 0.05 Hz) sine and cosine from the data to further subtract correlated noise contamination.

4.3. Mapmaking

Finally, we obtain surface brightness maps by projecting and averaging the signal from all KIDs on a pixelized map at 140 GHz. The projected data are weighted according to the level of noise of each detector using inverse variance weighting. In order to remove possible offsets in the TOD, we subtract the mean value of

each TODs and we take the zero level as the mean of the external part of the map, where no signal is detected.

4.4. Point source subtraction

RX J1347.51145 hosts a radio point source located within 3 arcsec of the X-ray center that has a flux of 4.4 ± 0.3 mJy and 3.2 ± 0.2 mJy at 140 and 240 GHz respectively (Pointecouteau et al. 2001). The point source is subtracted in the TODs at both frequencies, before the data analysis so that it does not bias the analysis.

5. Validation of the analysis

We present two validations of the analysis pipeline. One is a detailed simulation of the observation of a tSZ cluster with known parameters and typical atmospheric and electronic noise. The other, based on the observation of a faint cluster, shows that the detection is not an artifact of the analysis or the data acquisition.

5.1. Simulation

In order to test the pipeline described in Sect. 4, we simulate the *NiKA* observations of a cluster and construct the TODs by taking into account all terms of Eq. 4, i.e. the atmospheric contamination, the electronic noise and the tSZ signal. The parameters used in the simulation are given in Tab. 3 and are representative of the weather conditions of the observations described in this paper.

5.1.1. Atmospheric contribution

The atmospheric contribution $A(\nu_b, t)$ is simulated as described in Sect. 4.

The water vapor fluctuations (i.e. $a_{\text{H}_2\text{O}}^{\text{fluc}} A_{\text{H}_2\text{O}}^{\text{fluc}}(t)$) are obtained by simulating a map of water vapor anisotropy that passes in front of the telescope aperture with a speed $v_{\text{H}_2\text{O}}$ at an altitude above the telescope $h_{\text{H}_2\text{O}}$. The power spectrum of this map is a power law with slope $\alpha_{\text{H}_2\text{O}}$. The amplitudes of the atmospheric fluctuation are then normalized to have a standard deviation over

Parameter	Value
$\nu_{\text{H}_2\text{O}}$	1 m/s
$h_{\text{H}_2\text{O}}$	3000 m
$\alpha_{\text{H}_2\text{O}}$	-1.35
$\tau_{140 \text{ GHz}}$	0.1
$\tau_{240 \text{ GHz}}$	0.12
$(F_{\text{H}_2\text{O}})_{140 \text{ GHz}}$	28 Jy/beam
$(F_{\text{H}_2\text{O}})_{240 \text{ GHz}}$	110 Jy/beam
$F_{\text{el}}(140 \text{ GHz})$	14 Jy/beam/K
$F_{\text{el}}(240 \text{ GHz})$	35 Jy/beam/K
T_{atmo}	233 K
$E_0(1 \text{ Hz}, 140 \text{ GHz})$	38 mJy/beam
$E_0(1 \text{ Hz}, 240 \text{ GHz})$	76 mJy/beam
β	-0.25
$N_0(140 \text{ GHz})$	29 mJy.s ^{1/2}
$N_0(240 \text{ GHz})$	57 mJy.s ^{1/2}
R_g	0.065 s ⁻¹

Table 3. Values of the parameters used in the simulation, see text for details.

the time of the scan equal to $\sigma = F_{\text{H}_2\text{O}} \left(1 - \exp\left(-\frac{\tau}{\sin(\ell)}\right)\right)$ where τ is the zenith opacity, ℓ the elevation and $F_{\text{H}_2\text{O}}$ is the reference flux.

The contribution of the elevation terms, both from H_2O and O_2 , is simulated as

$$d_{\text{el}}(t) = F_{\text{el}} T_{\text{atmo}} \left(\exp\left(-\frac{\tau}{\sin(\ell)}\right) - \exp\left(-\frac{\tau}{\sin(\ell)}\right) \right) \quad (6)$$

The parameter T_{atmo} is the temperature of the atmosphere and F_{el} a reference flux that is measured at both frequencies using skydips.

5.1.2. Electronic noise

The electronic noise $E(\nu_b, t)$ is simulated as a common-mode with power spectrum slope β and an amplitude E_0 . This common-mode is identical for all detectors in a given frequency band but differs for the two bands since the electronics is not the same. The spectrum slope is the same for the two bands but the amplitude is higher at 240 GHz than 140 GHz (see Tab. 3).

5.1.3. Simulation of the intrinsic detector noise

The intrinsic noise of the detectors $N_k(t)$ accounts for all the sources of non correlated white noise that limit the sensitivity (e.g. photon noise, spontaneous Cooper pair breaking due to thermal noise, electronics, ...). It is supposed to be independent of the observing conditions³. The amplitude of the noise N_0 is assumed to be identical for all detectors of one array.

5.1.4. The glitches

Glitches are simulated with a rate R_g . They only affect individual samples in the TODs (i.e. the KID response is much faster than the sampling frequency) and affect simultaneously all KIDs of a given array (i.e. glitches are assumed to generate phonons that

³ In practice, some detectors are background limited. Moreover, the instrumental noise depends on the atmospheric conditions via the shape of the resonances that broaden under larger optical load, i.e. the instrumental noise increases with the opacity.

	Compact cluster	Diffuse cluster
P_0 (keV/cm ³)	3.28	0.50
(α, β, γ)	(0.9, 5.0, 0.0)	(0.9, 5.0, 0.0)
r_s (kpc)	406	1500
θ_s (arcsec)	70	259

Table 4. Generalized NFW parameters used to simulate the compact and diffuse clusters.

hit all the KIDs of the array). The amplitudes of the glitches are generated using a gaussian spectrum with a standard deviation of 1.3 Jy/beam as observed in the measured TODs.

5.1.5. Pulse tube lines

In order to simulate the frequency lines generated by the pulse tube, we add cosine functions to the timeline that correspond to the typical frequencies and amplitudes seen in the data (see the power spectrum of the raw data in Fig. 3).

5.1.6. The thermal Sunyaev Zel'dovich signal

We use the generalized Navarro, Frenk and White (gNFW) pressure profile (Nagai et al. 2007b) in order to describe the cluster pressure distribution out to a significant fraction of the virial radius. This profile is given by

$$P(r) = \frac{P_0}{\left(\frac{r}{r_s}\right)^\gamma \left(1 + \left(\frac{r}{r_s}\right)^\alpha\right)^{\frac{\beta-\gamma}{\alpha}}} \quad (7)$$

where P_0 is a normalizing constant; α , β and γ set the slope at intermediate, large and small radii respectively and r_s is the characteristic radius. The same profile can be written in its universal form (Arnaud et al. 2010) by relating the characteristic radius to the concentration parameter c_{500} , $r_s = r_{500}/c_{500}$, with r_{500} the radius within which the mean density of the cluster is equal to 500 times the critical density of the Universe at the cluster redshift. The pressure normalization can then be written as $P_0 = P_{500} \times \mathbb{P}_0$, where \mathbb{P}_0 is a normalization factor and P_{500} is the average pressure within the radius r_{500} , related to the average mass within the same radius, M_{500} , by a scaling law. We finally define $\theta_s = r_s/D_A$ the characteristic angular size, where D_A is the angular diameter distance of the cluster.

We simulate two kinds of clusters. The first one is rather compact (peaked) and the second one is rather diffuse. The corresponding parametrization can be found in Tab. 4. Using these sets of parameters, we compute the Compton parameter map according to Eq. (3), integrating the pressure along the line-of-sight. The map is then convolved with the instrumental beam and converted into surface brightness. We use the same scanning strategy as in the case of RX J1347.5-1145 observations of *NIKA* during the Run 5. The focal plane and the number of detectors are also the same.

5.1.7. Validation of the pipeline on simulated data

After processing the simulated data, we recover the two cluster maps (compact and diffuse) shown in Fig. 4. We can observe that the clusters are detected with a signal to noise of the order of 10 and well mapped in both cases. The signal amplitude is slightly reduced with respect to the input maps (see Fig. 5).

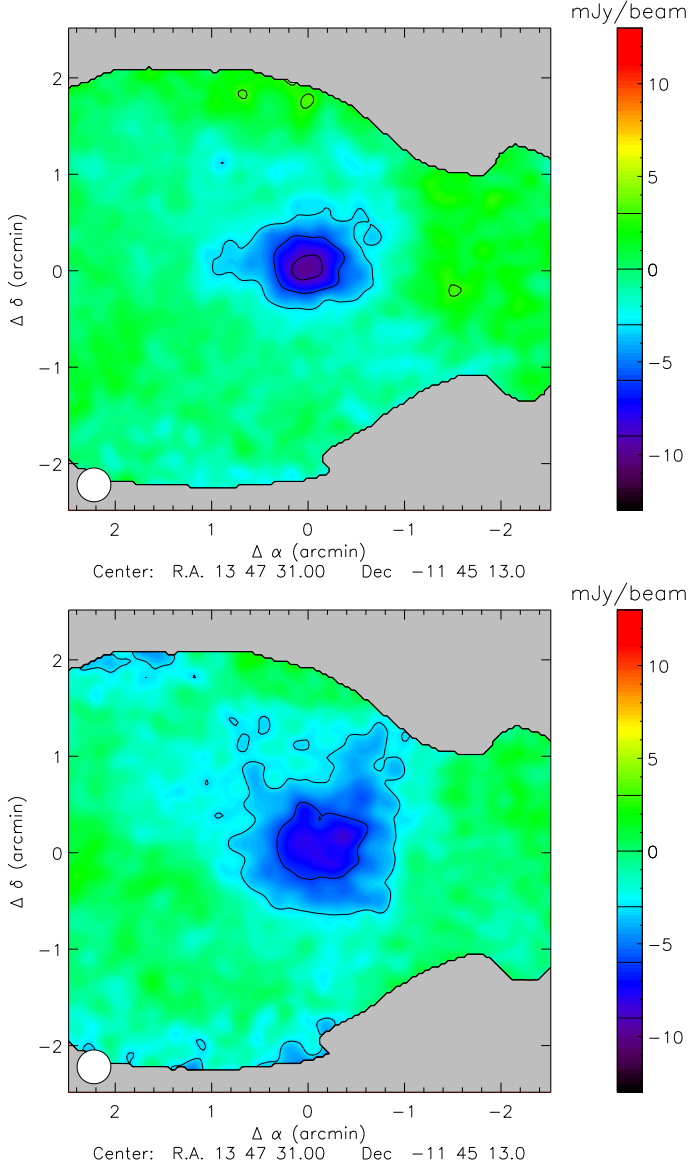


Figure 4. Generalized NFW simulations of two clusters processed through the pipeline. The first one is rather peaked (top panel) compared to the *NIKA* map, and the second one is more extended (bottom panel). The parameters used in the clusters simulation are given in Tab. 4. Note that the maps are shown up to a noise level that is twice the minimal noise level of the map. The effective beam is shown on the bottom left corner accounting for the instrumental beam and the 10 arcsec gaussian smoothing of the maps. The contours are 3, -3, -6 and -9 mJy/beam.

Using these maps, we compute the angular profiles of the recovered clusters by evaluating the average flux value for a set of concentric annuli. They are shown in Fig. 5 as green and red dots for the compact and diffuse clusters respectively. Comparison with the input profiles is provided by solid lines with similar colors. We also show the profiles recovered after projection only, in order to check zero level effects (orange and blue diamonds for the compact and diffuse cluster respectively).

First of all, due to the scanning strategy, the largest angular scale recovered in the map is 6 arcmin, the size of the observed map. This can be seen in Fig. 5 with the profile of the diffuse cluster (projection only; blue diamonds) which reaches the zero

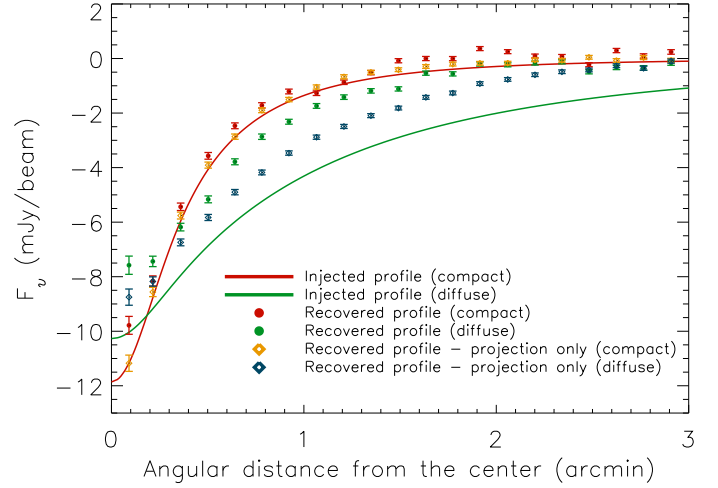


Figure 5. Comparison of the profiles injected in the simulation and recovered at the end of the pipeline. The injected profiles are given as red (compact cluster) and green (diffuse cluster) solid lines. The recovered profiles are shown with dots of similar colors. We also show the recovered profiles in the case of projection only without correlated noise, glitches or pulse tube lines included in the simulation. They are given as orange (compact cluster) and blue (diffuse cluster) diamonds.

level at 3 arcmin, unlike the injected profile that extends further. Then, the processing affects the map in the case of the diffuse cluster by reducing the measured flux up to 15% at radii of ~ 1 arcmin. The shape of the profile is not affected in the case of the compact cluster. Finally, the remaining correlated noise can slightly contaminate the profile but it is not significant once averaged on concentric annuli.

5.2. Map of the undetected galaxy cluster IDCS J1426.5+3508

In Fig. 6, we show the map obtained by mapping IDCS J1426.5+3508, a faint, high redshift ($z = 1.75$), cluster of galaxies. The expected tSZ decrement is ~ 0.25 mJy/beam at 140 GHz, with an angular size of ~ 2 arcmin (Brodwin et al. 2012). We therefore expect a non-detection since its flux is below the standard deviation of the noise of our map at the cluster location by a factor of ~ 5 . This target has been chosen in order to verify that the tSZ signal observed in RX J1347.5-1145 data is not due to a bias in the analysis.

IDCS J1426.5+3508 has been observed for 5 hrs 41 min of unflagged on-source data in atmospheric conditions slightly poorer but comparable to those described in Tab. 1 for RX J1347.5-1145. The map obtained does not show any evidence of tSZ signal and is consistent with the noise as expected.

6. Results

6.1. RX J1347.5-1145 as observed by *NIKA*

Fig. 7 presents the tSZ map obtained with the *NIKA* prototype. The radio source is not subtracted from this map. The associated difference map of separated equivalent subsamples (Jack-Knife), normalized by a factor of 2 to preserve the statistical properties of the noise in the tSZ map, is given in the left panel of Fig. 8. We also present on the right panel the histogram of the pixel values. The contour of the maps shown is defined by the limit

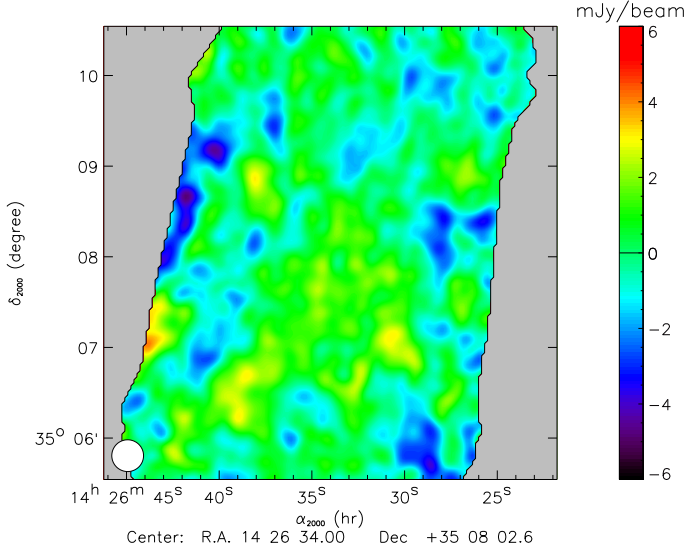


Figure 6. Map at 140 GHz of the undetected galaxy cluster IDCS J1426.5+3508.

where the statistical noise level, that increases toward the edges of the full map, equals twice the minimum noise level of the inner region. The bottle-like shape of the cut-off is due to the scan strategy detailed in Sect. 3.2. The non homogeneity of the noise can be seen directly on the map of Fig. 8 using the $\pm 1 < \sigma >$ contours, with $< \sigma >$ being the averaged root mean square of the noise map within the cutoff (the map unmasked). The difference map gives a direct estimation of the root mean square of the noise in the cluster map of $< \sigma > = 1.11$ mJy/beam. This is done by fitting the histogram of the pixel value with a gaussian distribution. The contours of the tSZ map of Fig. 7 correspond to 3, -3, -6 and -9 mJy/beam with the noise level being $1\sigma \approx 1$ mJy/beam at the cluster location. The beam is shown on the bottom left corner of the map, accounting for both the 18.5 arcsec instrumental beam and the extra 10 arcsec gaussian smoothing of the map (*i.e.* 21 arcsec). In terms of Compton parameter, the map gives the sensitivity of the *NIKA* prototype camera, during the campaign of November 2012, of $\sim 10^{-4} \sqrt{h}$ for one beam and 1σ .

We can see clearly the tSZ decrement that reaches up to $\approx 10\sigma$. The signal is extended and does not coincide with the X-ray center, (R.A, Dec) = (13h 47m 30.59s, -11° 45' 10.1"), as expected from the merger (see Sect. 2). The tSZ maximum corresponds to the shock location, but even on scales as large as 1.5 arcmin, the tSZ signal is larger on the south/south-east side of the map. The tSZ maximum corresponds to $\approx 10^{-3}$ in units of Compton parameter y , as expected for this cluster according to Pointecouteau et al. (1999). This is also consistent with *CARMA* result (Plagge et al. 2012) as discussed in Sect. 7.

6.2. RX J1347.5-1145 profile

Fig. 9 gives the flux profile as a function of the angular distance extracted from the tSZ map of Fig. 7. In the case of RX J1347.5-1145, the tSZ barycenter and the X-ray center do not coincide due to the ongoing merger. Therefore, we compare on the left panel the profile computed from the X-ray center, (R.A, Dec) = (13h 47m 30.59s, -11° 45' 10.1"), and the tSZ peak taken to be at the coordinates (R.A, Dec) = (13h 47m 31s, -11° 45' 30") from the maximum decrement of the *NIKA* map. The error bars have been computed from the simulations of noise

maps with statistical properties estimated using the difference map of the left panel of Fig. 8.

The right panel of Fig. 9 compares the profile of RX J1347.5-1145 from the X-ray center in three different areas: the North-West, the North-East and the South. It does indeed show the increase in thermal pressure in the southern region, where the subclump (merging) is observed in X-ray and tSZ (Sect. 2). This is due to the compression of the hot gas within the merging process which increases the temperature and thus the pressure (deepening the tSZ decrement at 140 GHz). Note that the southern extension coincide with the presence of a radio mini-halo (see the work by Gitti et al. 2007a) which implies the presence of non-thermal electrons which could underline a non-thermal contribution to the total pressure (not seen in the tSZ signal).

Note that the radio source is subtracted before the calculation of the profiles since we focus on the pressure distribution of the cluster.

6.3. Modeling of the cluster pressure profile

RX J1347.5-1145 has been intensively studied in X-rays, it looks fairly regular at large scale down to the center in the north direction, with a low central entropy (Cavagnolo et al. 2009). The contrast with the southern part, which shows a tSZ and X-ray extension, suggests that RX J1347.5-1145 was a spherical, relaxed, cool-core cluster that has been subject to the merging of a subcluster on its southern part. We therefore aim at quantifying the tSZ South East extension detected with the *NIKA* prototype by modeling and subtracting the signal coming from the relaxed region, located on the northern-west side of the X-ray center. We have then modeled the tSZ signal by considering a gNFW profile (Eq. 7), centered at the X-ray position of the system, whose inner, outer and intermediate slopes (γ, β, α) have been set equal to the cool-core best fitting values of Arnaud et al. (2010) ($\gamma_{cc} = 0.7736, \beta_{cc} = 5.4905, \alpha_{cc} = 1.2223$). In order to obtain the best fitting values of P_0 and θ_s , we have used a Markov Chain Monte Carlo (MCMC) approach. The sequence of random samples, the chain, has been built by implementing the Metropolis-Hasting algorithm (Chib & Greenberg 1995), which means that the parameter space is explored with a trial step drawn from a symmetric probability distribution. Convergence is checked by including the test proposed by Gelman & Rubin (1992).

The parameters P_0 and θ_s have been constrained by masking the South East extension. The mask has been defined as a half ring on the southern part of the cluster, centered on the X-ray peak with inner and outer radii set respectively to 10 and 80 arcsec. By masking the hottest region of the system, the constraints obtained on the best fit parameters are mainly driven by the cool-core like component, where the cluster temperature stays below 10 keV. Consequently, the flux relativistic correction (Itoh et al. 1998) is estimated to be $\lesssim 7\%$ for the channel at 140 GHz, and it is thus neglected. The best fit parameters obtained are

$$\begin{aligned} P_0 &= 0.198 \pm 0.028 \text{ (stat.) } \pm_{0.037}^{0.054} \text{ (syst.) keV/cm}^3 \\ \theta_s &= 1.510 \pm 0.093 \text{ (stat.) } \pm_{0.00}^{0.30} \text{ (syst.) arcmin} \end{aligned} \quad (8)$$

The corresponding posterior likelihood is given in Fig. 10 and accounts only for statistical uncertainties. The systematic uncertainties have been computed using the calibration uncertainty and taking into account bias filtering effect of the analysis estimated from the difference in the input and output simulated profiles. P_0 is affected symmetrically by the calibration uncertainty while the negative bias (lowering the true value) has been

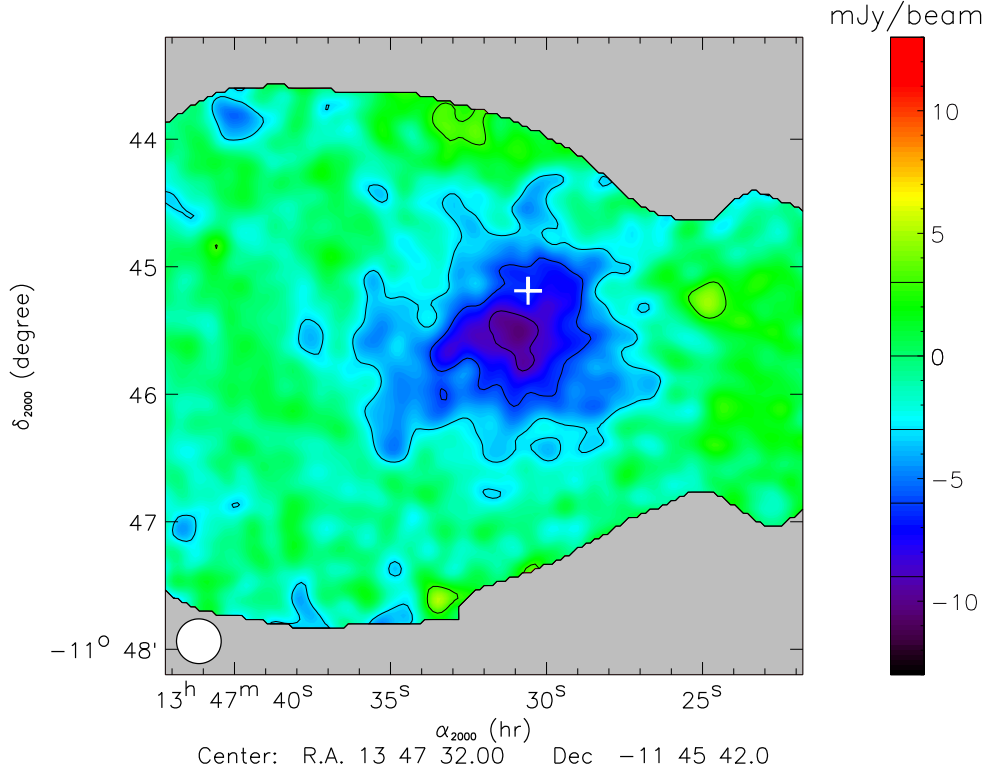


Figure 7. NIKA map of RX J1347.5-1145 at 140 GHz. The map is given in mJy/beam. It is clipped up to a root mean square noise level that is twice the minimum of the map as detailed in the text. The contours are at 3, -3, -6 and -9 mJy/beam with $1\sigma \cong 1$ mJy/beam at the cluster location. The minimum value of the map corresponds to $y \approx 10^{-3}$. The X-ray center location is represented by a white cross. The radio source location also corresponds to the white cross within 3 arcsec.

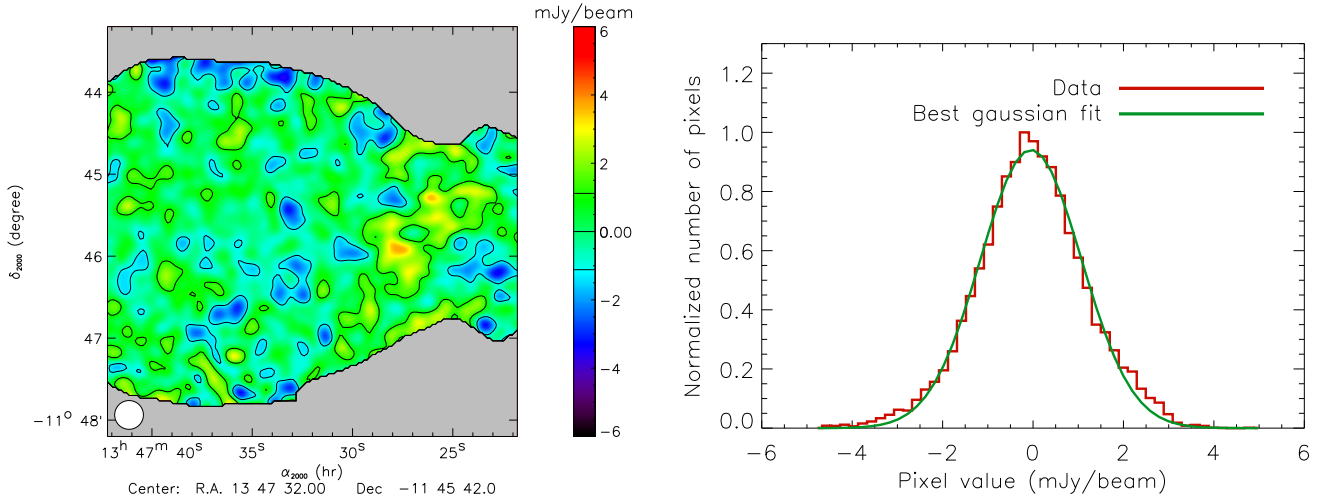


Figure 8. RX J1347.5-1145 observations. Left: difference map of two equivalent subsamples normalized by a factor of 2 to mimic the noise properties of the tSZ map. The pixels are 2×2 arcsec and the map has been smoothed with a 10 arcsec gaussian filter, similarly to the tSZ map of Fig. 7. Right: distribution of the value of the pixels in the difference map. The gaussian fit of the histogram gives the mean value of the standard deviation of the map shown in Fig. 7. We have on average $\langle \sigma \rangle = 1.11$ mJy/beam and the minimum noise level reaches up to 0.8 mJy/beam. The contours of the noise map correspond to $\pm \langle \sigma \rangle$. We can observe that the noise level is not homogeneous, being lower on the left hand side due to the differences of acquisition time.

estimated to less than 20%. θ_s is only affected by the bias, estimated to less than 20%, lowering its true value. Note that in the case of no mask being applied to the map, θ_s is larger by about 0.1 arcmin, but still compatible with the value given above, reinforcing the confidence in the value obtained. Similarly, assuming the best fit slope parameters of the stacked *Planck* clusters (Planck Collaboration et al. 2012) ($\gamma_{Planck} = 0.31, \beta_{Planck} = 4.13$,

$\alpha_{Planck} = 1.33$) returns a best fit flux density profile compatible within error bars.

Fig. 11 gives the comparison between the NIKA prototype – point source subtracted – map (left panel), the best fit model obtained for the relaxed component (middle panel), and the residual (right panel). The model represents well the northern part of the tSZ map but the southern side cannot be explained without

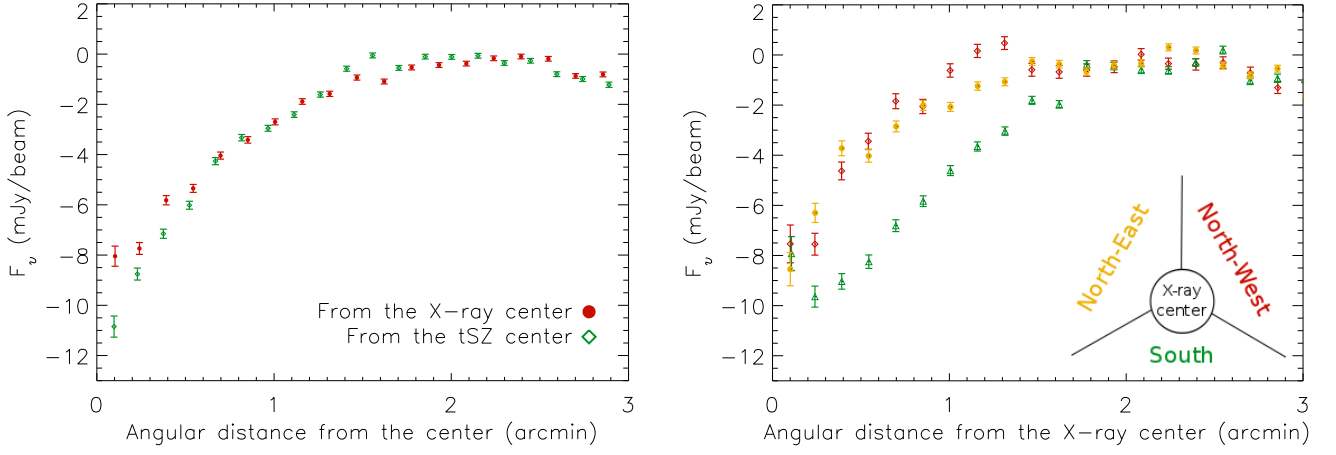


Figure 9. Radial flux profiles of RX J1347.5-1145. Left: comparison of the radial profile computed from the X-ray (red dots) and tSZ (green diamonds) centers. Right: comparison of the radial flux profile in three different regions, from the X-ray center. The map is cut from the X-ray center in three equal slices, one cut is vertical coming from the north to the center and the two others are diagonal from the south east and the south west to the center respectively. The red diamonds and yellow dots profiles correspond respectively to the North-West and North-East part of the map, where the cluster is expected to be rather relaxed. The green triangle profile corresponds to the southern part of the map, where the merging occurred.

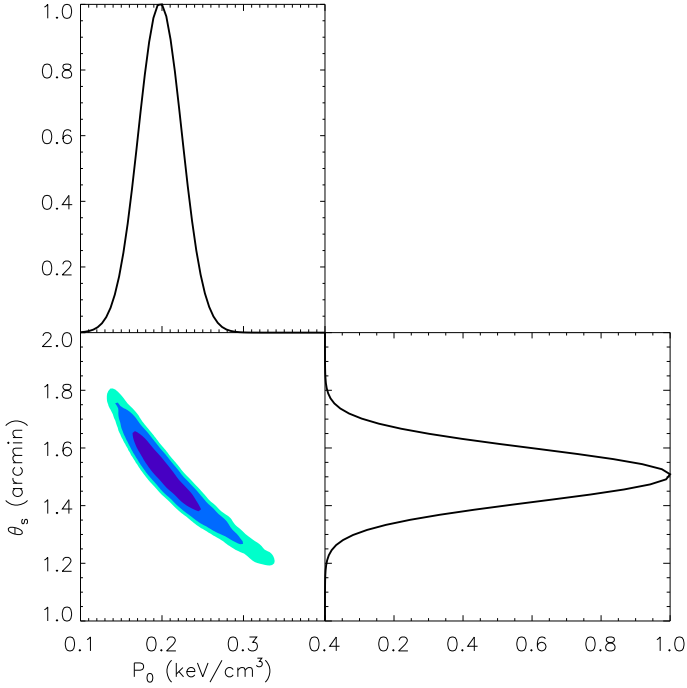


Figure 10. Posterior likelihood of the MCMC pressure profile fit in the plane $P_0 - \theta_s$. From dark to light blue, the colors correspond to 68%, 95% and 99% confidence levels. The top and right curves show the normalized gaussian best fit of the marginalized likelihood of P_0 and θ_s respectively.

including an overpressure component, that is known to be due to the merging of a subcluster (see Sect. 2).

The best fit model and the residual tSZ map given in Fig. 11 have been used to quantify the distribution of the signal within the region where the intra-cluster gas is more relaxed towards hydrostatic equilibrium and the region where it is expected to be shock heated. For this purpose, we compute the integrated

Compton parameter, defined as

$$Y_{\theta_{\max}} = \int_{\Omega(\theta_{\max})} y d\Omega, \quad (9)$$

over the solid angle Ω up to the radius θ_{\max} from the X-ray center. This is done separately on the best fit model map (Fig. 11, middle panel) and the residual (Fig. 11, right panel). Given the size of our map, we decided to integrate up to $\theta_{\max} = 2$ arcmin, obtaining, $Y_{\theta_{\max}}^{\text{cc}} = (1.09 \pm 0.20) \times 10^{-3}$ arcmin² and $Y_{\theta_{\max}}^{\text{shock}} = (0.64 \pm 0.12) \times 10^{-3}$ arcmin². Thus, the total integrated Compton parameter is $Y_{\theta_{\max}}^{\text{total}} = (1.73 \pm 0.32) \times 10^{-3}$ arcmin². The shock contribution to the tSZ signal is estimated to be 37% within the 2 arcmin radius.

7. Comparison to other external data sets

7.1. Comparison to the Planck catalogue of tSZ sources

The overall integrated Compton parameter for RX J1347.5-1145 can be compared to the *Planck* satellite measurement reported in the *Planck* catalogue of tSZ sources (Planck Collaboration et al. 2013a). For each detection, the *Planck* catalogue provides the two-dimensional $\theta_s - Y_{5R_{500}}$ probability distribution. θ_s is again the characteristic radius of Eq. 7 and $Y_{5R_{500}}$ is the integrated Compton parameter within a radius equal to $5 \times r_{500}$, therefore assumed to be the total flux. The catalogue contains also the slopes of the gNFW pressure profile used by the detection pipeline, allowing us to compute the $Y_{\theta_{\max}} / Y_{5R_{500}}$ ratio, and so to reconstruct the *Planck* flux ($Y_{5R_{500}}$) to the integrated signal at any cluster centric distance ($Y_{\theta_{\max}}$). In order to compare our result to *Planck* data, we have explored here two different methodologies.

On the one hand we fixed θ_s to its maximum likelihood value, obtaining $Y_{5R_{500}} = (2.17 \pm 0.36) \times 10^{-3}$ arcmin² for RX J1347.5-1145. Then, the $Y_{\theta_{\max}} / Y_{5R_{500}}$ ratio returns $Y_{\theta_{\max}}^{\text{Planck}} = (1.78 \pm 0.30) \times 10^{-3}$ arcmin², for $\theta_{\max} = 2$ arcmin, which is in good agreement with the *NIKA* value, $Y_{\theta_{\max}}^{\text{total}} = (1.73 \pm 0.32) \times 10^{-3}$ arcmin².

On the other hand, the *Planck* tSZ angular size (θ_s) – flux ($Y_{5R_{500}}$) degeneracy can also be broken by fixing r_{500} to its

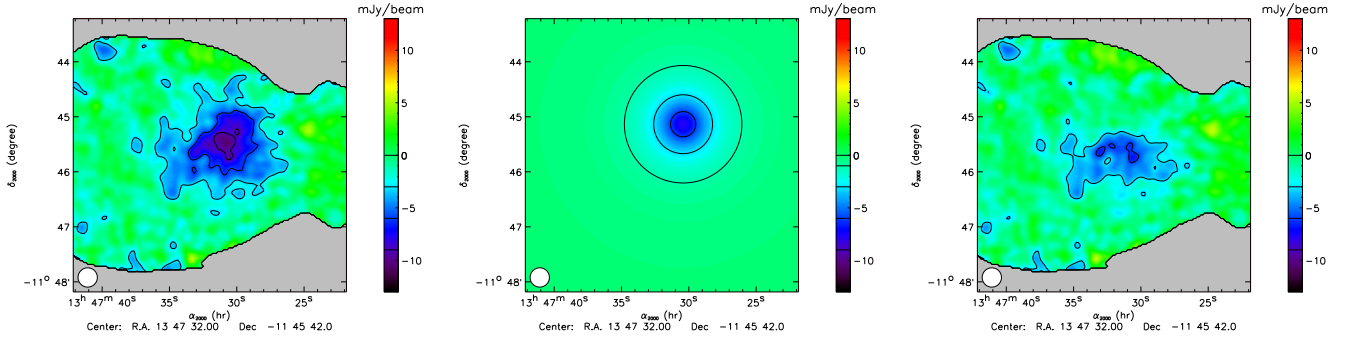


Figure 11. Comparison between the original point source subtracted RX J1347.5-1145 tSZ map (left panel) and the best fit model map excluding the shock area (middle panel). The residuals are given on the right panel map. The model accounts well for the cluster profile except in the southern shocked area as expected.

X-ray derived value, without changing the other pressure profile parameters, including c_{500} (which is kept equal to 1.1733, the value given by Arnaud et al. 2010). This is what Planck Collaboration et al. 2013a uses when recovering the integrated tSZ signal within the X-ray size. Following this approach we obtain $Y_{\theta_{\max}}^{\text{Planck}} = (1.23 \pm 0.21) \times 10^{-3} \text{ arcmin}^2$, for $\theta_{\max} = 2 \text{ arcmin}$. This value, although weaker, is still consistent with *NIKA* flux. Nevertheless, the latter can be understood if we consider that the X-ray derived $r_{500} = 1.42 \text{ Mpc} \equiv \theta_{500} = 3.94 \text{ arcmin}$ (*MCXC*, Piffaretti et al. 2011) is much larger than the reliable radial extent of the *NIKA* map. The r_{500} that can be deduced from the *NIKA* θ_s parameter is instead smaller. However we expect the two integrated Compton parameters to converge when we move to larger θ_{\max} . Indeed, when pushing the integration up to $\theta_{\max} = 2.5 \text{ arcmin}$ (extrapolating the best-fit model of the relaxed region to angular distances not directly probed through our observations and assuming that the contribution due to the shock is negligible at scales larger than $\sim 2 \text{ arcmin}$), we obtain $Y_{\theta_{\max}}^{\text{Planck}} = (1.52 \pm 0.26) \times 10^{-3} \text{ arcmin}^2$ versus $(1.77 \pm 0.33) \times 10^{-3} \text{ arcmin}^2$ for *NIKA*. Alternatively, the larger *NIKA* flux can also be explained by relaxing the constant c_{500} hypothesis. The different sensitivities of *Planck*+*MCXC* and *NIKA* to the signal distribution could in fact lead to differences in the recovered flux distribution. With r_{500} fixed to its X-ray value, a larger c_{500} implies a smaller θ_s and therefore that a larger fraction of the total tSZ flux is located within the innermost regions. In this case, we would have a better consistency between the *Planck*+*MCXC* versus *NIKA* integrated Compton parameter even at smaller cluster-centric distances. Since the value of $c_{500} = 1.1733$ has been obtained on an average (universal) profile (Arnaud et al. 2010), and RX J1347.5-1145 is known to be very peaked compared to other clusters, this hypothesis is likely to be correct: the inner slope parameter γ being fixed, c_{500} can typically vary from ~ 0 to ~ 5 between clusters (Planck Collaboration et al. 2013e).

We can then conclude that, despite the large angular scale cutoff (above 3 arcmin), *NIKA* is able to recover most of the tSZ signal. The *Planck* – *NIKA* complementarity will be even more interesting and easily exploitable with the larger field of view (6.5 arcmin) that the *NIKA2* camera will reach.

7.2. Comparison to *DIABOLO* tSZ observations

We present in Fig. 12 the comparison between *DIABOLO* and the *NIKA* results on RX J1347.5-1145. *DIABOLO* (Pointecouteau et al. 1999, 2001) was a bolometric camera that observed RX J1347.5-1145 at the IRAM 30-meter telescope us-

ing a dual-band instrument at frequencies corresponding to the *NIKA* prototype bands: 140 and 250 GHz. The resolution of *DIABOLO* was 22 arcsec at 140 GHz. The data reduction and the instrumental similarities with *NIKA* make it a perfect choice for a direct comparison.

The left panel shows the tSZ *NIKA* map with *DIABOLO* contours overplotted in red with levels -1, -3, -5 and -7 mJy/beam (radio source not subtracted in both maps). We can see that the tSZ maxima and the external part of the cluster match within error bars. The overall amplitude of the signal is slightly higher for *NIKA* data than for *DIABOLO*. However, this difference is not significant once we account for the systematic uncertainties given in Tab. 2. The right panel of Fig. 12 gives the comparison of the radio source subtracted, X-ray centered, measured profiles with both instruments. The two profiles are compatible within error bars over the whole radial range, even though *NIKA* seems to detect more signal in the inner part of the cluster. The reduced χ^2 associated to the profile difference, computed up to a radius of 2.5 arcmin, is equal to 2.35. However, since this does not account for calibration uncertainties, we also give the reduced χ^2 after cross calibrating the two profiles: we obtain $\chi^2 = 1.32$ with a cross-calibration factor of 1.09, compatible with our calibration error estimate. In both cases, the tSZ maximum is not located at the X-ray center, as expected.

7.3. Comparison to *XMM* and *Chandra* X-ray observations

XMM data (Jansen et al. 2001) have been used to compute a number count map of RX J1347.5-1145 that we compare to the *NIKA* tSZ observations. As we can see on the left panel of Fig. 13, the tSZ peak does not coincide with the X-ray center. RX J1347.5-1145 gives a striking example of the power of tSZ data and its complementarity with X-ray. Indeed, the map of Fig. 13 shows that the *NIKA* prototype is able to probe the ICM at larger radii than X-ray data. Moreover, the mismatch between the tSZ and X-ray center gives precious information on the gas physics at play in the ICM.

The higher resolution of the *Chandra* X-ray data has instead been used for cluster simulation purposes. In particular, the work of Comis et al. (2011) uses the publicly available, X-ray derived, pressure profiles of the ACCEPT (Archive of *Chandra* Cluster Entropy Profile Tables) clusters (Cavagnolo et al. 2009) to constrain the P_0 , r_s and γ parameters of the gNFW pressure profile (Eq. 7). The best-fitting values obtained for RX J1347.5-1145 (Tab. 5) have been used in the present work to simulate the expected tSZ signal, as explained in Sect. 5.1.6. Once processed through the pipeline, the expected profile is compared to the

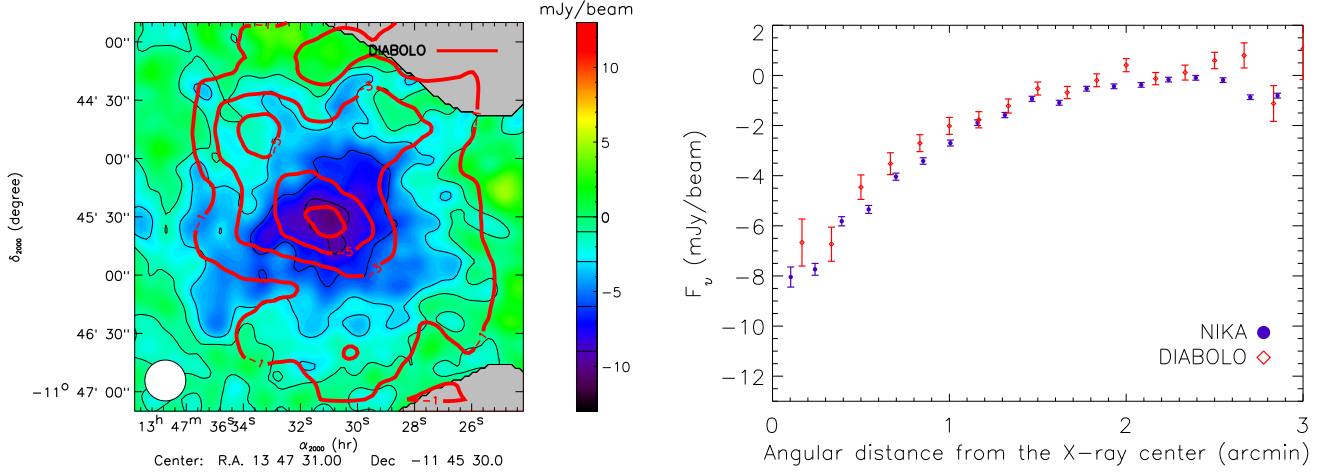


Figure 12. Comparison of RX J1347.5-1145 tSZ maps by *DIABOLO* and *NIKA* in mJy/beam. The left panel gives the *NIKA* tSZ map with *DIABOLO* contours in red at -1, -3, -5 and -7 mJy/beam. On the right panel is shown the flux radial profile as measured by the *NIKA* prototype (purple dots) and *DIABOLO* (red diamonds).

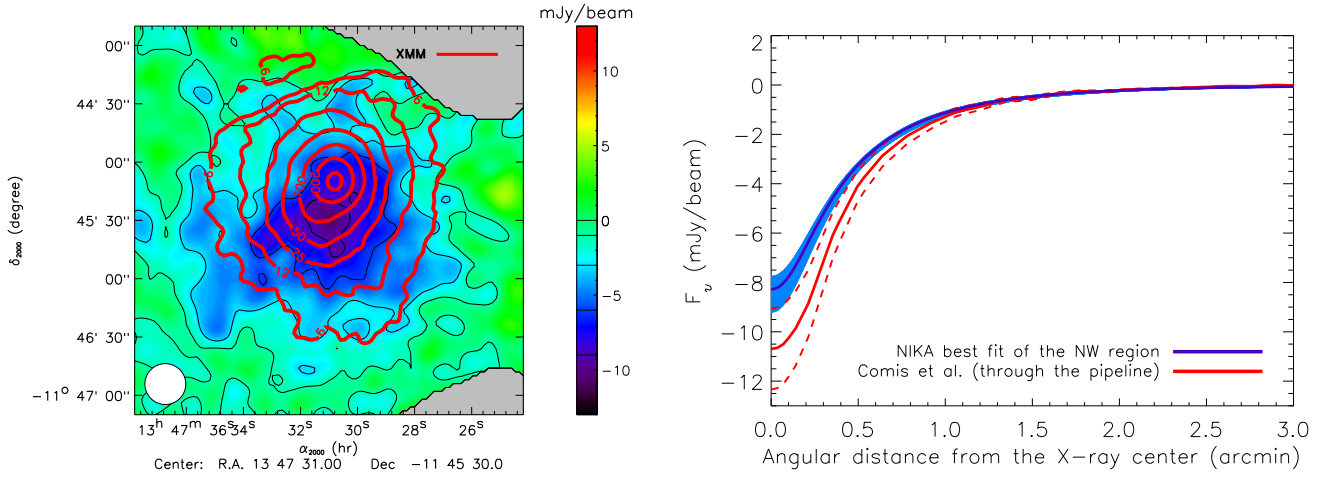


Figure 13. Left: comparison between the RX J1347.5-1145 *NIKA* tSZ map and the *XMM* X-ray data (see the work of Gitti & Schindler 2004, 2005; Gitti et al. 2007b). The *XMM* map has been smoothed with a 5 arcsec gaussian filter. The red X-ray contours are in number counts, they are given at levels of 6 12, 25, 50, 100, 200 and 400. Right: comparison between the best fit radial tSZ profile of the map measured by *NIKA* excluding the shock area (see Sect. 6.3) and the derived profile from *Chandra*'s data by Comis et al. (2011) once processed through the *NIKA* data reduction pipeline discussed in Sect. 4.2. The *NIKA* best fit profile is given in purple with associated 1σ statistical error range filled in blue and the X-ray model is given in red with the 1σ statistical error limit as two dashed lines. See text for more details on the errors limits.

NIKA best fit profile excluding the shocked area (see Sect. 6.3) on the right panel of Fig. 13. The *NIKA* best fit profile and the X-ray model are both given with associated 1σ error limit. The error on the *NIKA* profile accounts only for statistical uncertainties by sampling the 1σ contour of the likelihood of Fig. 10, the systematic errors (see Eq. 8) are not shown and would result in an overall multiplicative factors on the amplitude (P_0) and the angular scale (θ_s). We choose to include only the error on the parameter P_0 (Tab. 5) for the X-ray model since it is highly degenerated with θ_s and γ . In addition to the X-ray systematic uncertainties, the associated systematic error, which is not included in Fig. 13, arises mainly from the unit conversion coefficient (Jansky per beam to Compton parameter: $y = 10^{-3} \equiv 11.8 \pm 1.2$ mJy/beam). It has an effect similar to the error on the P_0 *NIKA* best fit value. The two profiles are in agreement within systematic and statistical uncertainties.

P_0 (keV/cm ³)	3.29 ± 0.50
(α, β, γ)	$(0.9, 5.0, 0.00 \pm 0.05)$
r_s (kpc)	406 ± 23
θ_s (arcsec)	70 ± 4

Table 5. Modeling of the pressure profile of RX J1347.5-1145 using the fit of *Chandra* data (Comis et al. 2011). Note that α and β have been fixed to the best-fitting values obtained by Nagai et al. (2007a), see Mroczkowski et al. (2009) for an errata.

7.4. Comparison to other high resolution tSZ data

We also compare the *NIKA* prototype data with state-of-the-art sub-arcmin resolution data: *MUSTANG* (Mason et al. 2010; Korngut et al. 2011) and *CARMA* (Plagge et al. 2012) observations. Since these two instruments are in many ways different from *NIKA*, we limit ourselves to a qualitative comparison.

MUSTANG uses the single dish 100-meter Green Bank Telescope in Virginia, USA. It operates at 90 GHz with a 8 arcsec resolution. Concerning RX J1347.5-1145, the central radio source is very bright compared to the tSZ decrement at 90 GHz. Once subtracted, the cluster reveals its substructures at high resolution with respect to the *NIKA* prototype. However, due to the fact that it is a single frequency instrument, the removal of the atmospheric noise filters angular scales larger than about 60 arcsec. In that sense, the *NIKA* prototype and *MUSTANG* are complementary. *MUSTANG* is able to measure the structural property of RX J1347.5-1145 at scales $\sim 10 - 60$ arcsec, while the *NIKA* prototype map is reliable in the range of $\sim 20 - 200$ arcsec. The two instruments agree on the morphology of RX J1347.5-1145 at intermediate scales (about the inner part of the -6 mJy contour on Fig. 7. The tSZ maximum coincides and the overall distribution of the tSZ signal are consistent on both observations. The excess seen in the region 2 of Fig. 5 in Mason et al. (2010) does not show up clearly in the *NIKA* map. However, the spatial scales of this feature is smaller than 10 arcsec thus it is likely smoothed out by the *NIKA* beam.

CARMA is a multi-frequency interferometer (Plagge et al. 2012). For RX J1347.5-1145 observations, it was made of 23 antenna of 3.5, 6.1 and 10.4 meter operating in three configurations at 31 GHz, 86 GHz and 90 GHz for a total of 41.7 hours of unflagged on-source observation. Due to the complexity of combining the data in different configurations, the *CARMA* transfer function is not simple. Nevertheless, *CARMA* and *NIKA* agree well on scales larger than about 30 arcsec and are consistent on smaller scales taking into account the complex beam of *CARMA*.

8. Conclusions and perspectives for *NIKA2*

RX J1347.5-1145 is an ongoing merger, amongst the most studied galaxy clusters at arcmin angular scales, making it a good target for the first tSZ observations with the *NIKA* prototype camera. Using a dual-band decorrelation together with a high resolution instrument, we have been able to image the tSZ morphology of the cluster from the core to its outer region. The detailed data analysis is specific to KIDs and has been validated on simulations. The observation of RX J1347.5-1145 constitutes the first tSZ observations with an instrument based on KIDs.

The reconstructed tSZ map of RX J1347.5-1145 is reliable on scales going from about 20 to 200 arcsec and shows a strong South East extension that corresponds to the merger shock. Indeed, we detect the non alignment of the tSZ maximum and the X-ray center, as expected from the overpressure caused by the ongoing merger. This is also observed in the radial flux profile of the cluster and the residual of the map with respect to the modeling of the relaxed part of the cluster. The generalized NFW fit of the NW region enables to constrain the cluster pressure profile parameters θ_s and P_0 . The pressure profile derived from X-ray is in good agreement with this tSZ best fit model.

The tSZ map and the radial profile measured with *NIKA* have been compared to *DIABOLO* observations at the same telescope and with similar resolution and frequency coverage. The agreement between the two maps validates the tSZ observations presented in this work. In addition, the *NIKA* prototype map agrees with state-of-the-art sub-arcmin resolution tSZ observations, *MUSTANG* (90 GHz and 8 arcsec resolution) and *CARMA* (30 – 90 GHz and ~ 15 arcsec resolution), and the comparison shows that it is complementary to these experiments.

In this paper, KID arrays in the *NIKA* prototype have been proved to be competitive detectors for millimeter wave astron-

omy and in particular for the observation of galaxy clusters via the tSZ effect. The next generation instrument, *NIKA2*, will be made of about 1000 detectors at 140 GHz and 4000 at 240 GHz with a field of view of ~ 6.5 arcmin. With these characteristics, *NIKA2* will be able to provide large high resolution mapping of clusters making it a perfect instrument for high resolution observation of intermediate to large distance clusters of galaxies. This will be well adapted for a follow-up of unresolved sources in the *Planck* cluster sample (Planck Collaboration et al. 2013a).

Acknowledgements. We would like to thank the IRAM staff for their support during the campaign. This work has been partially funded by the Foundation Nanoscience Grenoble, the ANR under the contracts "MKIDS" and "NIKA". This work has been partially supported by the LabEx FOCUS ANR-11-LABX-0013. This work has benefited from the support of the European Research Council Advanced Grant ORISTARS under the European Union's Seventh Framework Programme (Grant Agreement no. 291294). The *NIKA* dilution cryostat has been designed and built at the Institut Néel. In particular, we acknowledge the crucial contribution of the Cryogenics Group, and in particular Gregory Garde, Henri Rodenas, Jean Paul Leggeri, Philippe Camus. R. A. would like to thank the ENIGMASS French LabEx for funding this work. B. C. acknowledges support from the CNES post-doctoral fellowship program. E. P. acknowledges the support of grant ANR-11-BS56-015.

References

- Allen, S. W., Schmidt, R. W., & Fabian, A. C. 2002, MNRAS, 335, 256
- Arnaud, M., Pratt, G. W., Piffaretti, R., et al. 2010, A&A, 517, A92
- Basu, K., Zhang, Y.-Y., Sommer, M. W., et al. 2010, A&A, 519, A29
- Birkinshaw, M. 1999, Phys. Rep., 310, 97
- Böhringer, H. & Werner, N. 2010, A&A Rev., 18, 127
- Bourrion, O., Bideaud, A., Benoît, A., et al. 2011, JINST, 6, P06012
- Bradač, M., Schrabback, T., Erben, T., et al. 2008, ApJ, 681, 187
- Brodwin, M., Gonzalez, A. H., Stanford, S. A., et al. 2012, ApJ, 753, 162
- Calvo, M., Giordano, C., Battiston, R., et al. 2010, Experimental Astronomy, 28, 185
- Calvo, M., Roesch, M., Désert, F. X., et al. 2012, A&A
- Carlstrom, J. E., Ade, P. A. R., Aird, K. A., et al. 2011, PASP, 123, 568
- Carlstrom, J. E., Holder, G. P., & Reese, E. D. 2002, ARA&A, 40, 643
- Cavagnolo, K. W., Donahue, M., Voit, G. M., & Sun, M. 2009, ApJS, 182, 12
- Chib, S. & Greenberg, E. 1995, The American Statistician, 49, 327
- Cohen, J. G. & Kneib, J.-P. 2002, ApJ, 573, 524
- Comis, B., de Petris, M., Conte, A., Lamagna, L., & de Gregori, S. 2011, MNRAS, 418, 1089
- Day, P. K., LeDuc, H. G., Mazin, B. A., Vayonakis, A., & Zmuidzinas, J. 2003, Nature, 425, 817
- Doyle, S., Mauskopf, P., & Naylon, J. 2008, J. Low Temp. Phys., 151, 530
- Ferretti, L., Giovannini, G., Govoni, F., & Murgia, M. 2012, A&A Rev., 20, 54
- Gal, R. R. 2006, ArXiv Astrophysics e-prints
- Gelman, A. & Rubin, D. B. 1992, Statistical Science, 7, 457
- Gitti, M., Ferrari, C., Domainko, W., Ferretti, L., & Schindler, S. 2007a, A&A, 470, L25
- Gitti, M., Piffaretti, R., & Schindler, S. 2007b, A&A, 472, 383
- Gitti, M. & Schindler, S. 2004, A&A, 427, L9
- Gitti, M. & Schindler, S. 2005, Advances in Space Research, 36, 613
- Grabovskij, G. J., Swenson, L. J., Buisson, O., et al. 2008, Appl. Phys. Lett., 93, 134102
- Greve, A., Kramer, C., & Wild, W. 1998, A&AS, 133, 271
- Itoh, N., Kohyama, Y., & Nozawa, S. 1998, ApJ, 502, 7
- Jansen, F., Lumb, D., Altieri, B., et al. 2001, A&A, 365, L1
- Johnson, R. E., Zuhone, J., Jones, C., Forman, W. R., & Markevitch, M. 2012, ApJ, 751, 95
- Kitayama, T., Komatsu, E., Ota, N., et al. 2004, PASJ, 56, 17
- Kneib, J.-P. & Natarajan, P. 2011, A&A Rev., 19, 47
- Komatsu, E., Matsuo, H., Kitayama, T., et al. 2001, PASJ, 53, 57
- Korngut, P. M., Dicker, S. R., Reese, E. D., et al. 2011, ApJ, 734, 10
- Kosowsky, A. 2003, New A Rev., 47, 939
- Kravtsov, A. V. & Borgani, S. 2012, ARA&A, 50, 353
- Mason, B. S., Dicker, S. R., Korngut, P. M., et al. 2010, ApJ, 716, 739
- Miranda, M., Sereno, M., de Filippis, E., & Paolillo, M. 2008, MNRAS, 385, 511
- Monfardini, A., Benoît, A., Bideaud, A., et al. 2011, ApJS, 194, 24
- Monfardini, A., Swenson, L. J., Bideaud, A., et al. 2010, A&A, 521, A29
- Mroczkowski, T., Bonamente, M., Carlstrom, J. E., et al. 2009, ApJ, 694, 1034
- Mroczkowski, T., Dicker, S., Sayers, J., et al. 2012, ApJ, 761, 47

- Nagai, D., Kravtsov, A. V., & Vikhlinin, A. 2007a, *ApJ*, 668, 1
- Nagai, D., Vikhlinin, A., & Kravtsov, A. V. 2007b, *ApJ*, 655, 98
- NIKA Collaboration. 2013, in prep.
- Oliver, S. J., Bock, J., Altieri, B., et al. 2012, *MNRAS*, 424, 1614
- Ota, N., Murase, K., Kitayama, T., et al. 2008, *A&A*, 491, 363
- Pardo, J., Cernicharo, J., & Serabyn, E. 2002, in *Astronomical Society of the Pacific Conference Series*, Vol. 266, *Astronomical Site Evaluation in the Visible and Radio Range*, ed. J. Vernin, Z. Benkhaldoun, & C. Muñoz-Tuñón, 188
- Piffaretti, R., Arnaud, M., Pratt, G. W., Pointecouteau, E., & Melin, J.-B. 2011, *A&A*, 534, A109
- Plagge, T. J., Marrone, D. P., Abdulla, Z., et al. 2012, *ArXiv e-prints*
- Planck Collaboration, Ade, P. A. R., Aghanim, N., et al. 2013a, *ArXiv e-prints*
- Planck Collaboration, Ade, P. A. R., Aghanim, N., et al. 2013b, *ArXiv e-prints*
- Planck Collaboration, Ade, P. A. R., Aghanim, N., et al. 2013c, *ArXiv e-prints*
- Planck Collaboration, Ade, P. A. R., Aghanim, N., et al. 2013d, *ArXiv e-prints*
- Planck Collaboration, Ade, P. A. R., Aghanim, N., et al. 2012, *ArXiv e-prints*
- Planck Collaboration, Ade, P. A. R., Aghanim, N., et al. 2013e, *A&A*, 550, A131
- Pointecouteau, E., Giard, M., Benoit, A., et al. 1999, *ApJ*, 519, L115
- Pointecouteau, E., Giard, M., Benoit, A., et al. 2001, *ApJ*, 552, 42
- Roesch, M., Benoit, A., Bideaud, A., et al. 2012, *ArXiv e-prints*
- Schindler, S., Guzzo, L., Ebeling, H., et al. 1995, *A&A*, 299, L9
- Schindler, S., Hattori, M., Neumann, D. M., & Boehringer, H. 1997, *A&A*, 317, 646
- Staguhn, J., Allen, C., Benford, D., et al. 2008, *Journal of Low Temperature Physics*, 151, 709
- Sunyaev, R. A. & Zel'dovich, Y. B. 1972, *Astrophys. Space Phys. Res.*, 4, 173
- Sunyaev, R. A. & Zel'dovich, Y. B. 1980, *ARA&A*, 18, 537
- Swenson, L. J., Cruciani, A., Benoit, A., et al. 2010, *Appl. Phys. Lett.*, 96, 263511
- Verdugo, M., Lerchster, M., Böhringer, H., et al. 2012, *MNRAS*, 421, 1949